ELSEVIER

Aerospace Science and Technology 6 (2002) 171–183

Aerospace Science and Technology

www.elsevier.com/locate/aescte

Development and application of Spalart–Allmaras one equation turbulence model to three-dimensional supersonic complex configurations

Sébastien Deck *, Philippe Duveau, Paulo d'Espiney, Philippe Guillen

ONERA, 29, avenue Division Leclerc, 92322 Chatillon cedex, France

Received 1 June 2001; received in revised form 18 December 2001; accepted 11 January 2002

Abstract

This paper presents an extension of Spalart–Allmaras model to compressible supersonic flows. The model is implemented in a three-dimensionnal structured multi domain code using a high resolution implicit upwind scheme. Details of the formulation as well as the treatment of viscous gradients near boundaries are given. The method is validated for two different configurations. Firstly a cruciform missile simulation shows the ability of the method to capture accurately the interaction between the fuselage vortices and the winglets enabling the correct evaluation of the roll induced moment. Secondly an internal inlet flow computation including bleeds and struts demonstrates the usefulness and the accuracy of the method for multiple boundary layers supersonic complex configurations.

Keywords: Spalart–Allmaras model; Compressible supersonic flows

1. Introduction

Computational Fluid Dynamics (CFD) is playing an ever increasing role in missile aerodynamic design. The design of modern tactical supersonic missiles is heavily dependent upon the prediction of the vortical structures which appear along the leeward side of missiles bodies and inside the inlet. Accurate prediction of the flowfield, and more precisely the loss of total pressure in the core of the vortices, is all the more needed that they generally strongly interact with wings or control surfaces located downstream. CFD has definitively become an important tool in missile aerodynamic research.

Turbulence models play a key role when performing RANS simulations of turbulent flows. The prediction of flow phenomena such as boundary layer separation or shock boundary layer interaction depends strongly on the choice of the turbulence model. Algebraic models rely on equilibrium ideas to express directly the eddy viscosity in terms of known quantities of the mean flow. The well-known Baldwin Lomax model [4] has been widely used and has led to breakthrough of RANS simulations in industrial missile applications [6]. This model is cheap, robust and needs minimum requirements of computer time and storage which was particularly important in the past years. Nevertheless, as every algebraic model, it was built to calculate attached turbulent boundary layers, and some modifications have to be made to calculate other flowfields. Degani and Schiff [12] for instance proposed a modification in order to take the leeward vortices into account. A good review of such modifications for missiles can be found in Ref. [1,22]. Deck and Guillen [10] adapted an algebraic model to strong separated flows inside overexpanded nozzles.

Two equation models, even if they sometimes have to be aware of wall distances, can be formulated independently of the flow topology and with this respect are more suited to computations of complex geometries. Moreover, they take naturally into account history effects through transport equations, and are therefore considered to be more general. A large number of two equation models have been proposed in the literature. A good review of transport equation models capacities, like the standard k–ε model with low reynolds version of Jones–Launder [18], can be found in Deniau's thesis [13]. His study on two equation models provides a classification for supersonic missile configuration and shows

* Corresponding author.
E-mail address: deck@onera.fr (S. Deck).

1270-9638/02/$ – see front matter
PII: S1270-9638(02)01148-3

Nomenclature

CA	Total axial force coefficient	T	Temperature
CAf	Skin friction coefficient	$\vec{V}$	Velocity
Cl	Roll moment coefficient	x, y, z	Physical Carthesian coordinate axes
CN	Normal force coefficient	α	Angle of attack (degree)
Cp	Pressure coefficient	γ	Ratio of specific heats
D	Diameter of the fuselage	μ, μ_t	Laminar, eddy viscosities
E	Total energy	ρ	Density
M	Mach number	BL	Baldwin–Lomax model
P	Static pressure	DG	Degani–Schiff modification
P_0	Total pressure	SA	Spalart–Allmaras model

that some models can be difficult to implement in a general way. Moreover, boundary wall conditions are not always straightforward and can influence stability and accuracy of calculations. These numerical problems restrict their general application.

One equation models such as the Spalart–Allmaras model [25,26] or the Baldwin–Barth model [3] seem to be a good compromise between algebraic and two equation models. In particular, the Spalart–Allmaras model which solves directly a transport equation for the eddy viscosity, became quite popular because of its reasonable results for a wide range of flow problems and its numerical properties. This model has given good results for transonic turbulent flow in complex industrial configuration [16,24] and for slightly separated flow in overexpanded nozzles [11]. Nevertheless, not so many publications are devoted to investigations of the Spalart–Allmaras model behaviour in supersonic configurations. In order to try to fill this lack of knowledge, a numerical study of the Spalart–Allmaras model in two typical internal and external supersonic configurations has been undertaken.

The Spalart–Allmaras model and its different forms used in this study are described in Section 2. Section 3 concerns the numerical scheme and some implementation details are discussed. The last section relies on numerical aerodynamic calculations of industrial configurations of increasing complexity.

2. Turbulence modelling

2.1. First version of the model

The Spalart–Allmaras model [25] is a transport equation model for the eddy viscosity. The differential equation is derived by "using empiricism and arguments of dimensional analysis, Galilean invariance and selected dependence on the molecular viscosity". This model does not require finer grid resolution than the one required to capture the velocity field gradients with algebraic models. The transport equation for the working variable $\tilde{\nu}$ is given by:

$$\frac{\partial \tilde{\nu}}{\partial t} + \tilde{u}_j \frac{\partial \tilde{\nu}}{\partial x_j} = \underbrace{c_{b1}\widetilde{S}\tilde{\nu}}_{\text{Production}} + \underbrace{\frac{1}{\sigma}\left[\frac{\partial}{\partial x_j}\left((\nu+\tilde{\nu})\frac{\partial \tilde{\nu}}{\partial x_j}\right) + c_{b2}\frac{\partial \tilde{\nu}}{\partial x_j}\frac{\partial \tilde{\nu}}{\partial x_j}\right]}_{\text{Diffusion}} - \underbrace{c_{w1} f_w \left(\frac{\tilde{\nu}}{d}\right)^2}_{\text{Destruction}}. \tag{1}$$

The eddy viscosity is defined as

$$\mu_t = \bar{\rho}\tilde{\nu} f_{v1} = \bar{\rho}\nu_t. \tag{2}$$

In order to ensure that $\tilde{\nu}$ equals $\kappa y u_\tau$ in the log layer, in the buffer layer and viscous sublayer, a damping function f_{v1} is defined as:

$$f_{v1} = \frac{\chi^3}{\chi^3 + c_{v1}^3} \quad \text{with } \chi = \frac{\tilde{\nu}}{\nu}. \tag{3}$$

The vorticity magnitude S is modified such that $\widetilde{S}$ maintains its log-layer behaviour ($\widetilde{S} = \frac{u_\tau}{\kappa y}$):

$$\widetilde{S} = \sqrt{2\Omega_{ij}\Omega_{ij}} f_{v3} + \frac{\tilde{\nu}}{\kappa^2 d^2} f_{v2},$$
$$\Omega_{ij} = \frac{1}{2}\left(\frac{\partial \tilde{u}_i}{\partial x_j} - \frac{\partial \tilde{u}_j}{\partial x_i}\right) \tag{4}$$

which is accomplished with help of the functions:

$$f_{v2} = 1 - \frac{\chi}{1 + \chi f_{v1}}, \qquad f_{v3} = 1. \tag{5}$$

In order to obtain a faster decaying behaviour of destruction in the outer region of the boundary layer, a function f_w is used:

$$f_w(g) = g\left(\frac{1 + c_{w3}^6}{g^6 + c_{w3}^6}\right)^{1/6},$$
$$g = r + c_{w2}\left(r^6 - r\right), \quad r = \frac{\tilde{\nu}}{\widetilde{S}\kappa^2 d^2}, \tag{6}$$

where g acts as a limiter that prevents large values of f_w. Both r and f_w are equal to 1 in the log-layer and decrease in the outer region. Constants of the model are:

$$c_{b1} = 0.1355, \qquad c_{b2} = 0.622, \qquad \sigma = \frac{2}{3},$$
$$\kappa = 0.41, \qquad c_{w1} = \frac{c_{b1}}{\kappa^2} + \frac{1 + c_{b2}}{\sigma}, \qquad c_{w2} = 0.3,$$
$$c_{w3} = 2, \qquad c_{v1} = 7.1. \tag{7}$$

2.2. Spalart's modifications

Some cases showed poor convergence of the residual turbulence especially near reattachment. The problem was traced to $\widetilde{S}$ going negative which disturbed r and resulted in blinking. Spalart has proposed the following modifications of his model:

$$\widetilde{S} = \tilde{f}_{v3}(\chi) S + \frac{\tilde{\nu}}{\kappa^2 d^2} \tilde{f}_{v2}(\chi) \quad \text{with}$$
$$\tilde{f}_{v2}(\chi) = \left(1 + \frac{\chi}{c_{v2}}\right)^{-3},$$
$$\tilde{f}_{v3}(\chi) = \frac{(1 + \chi f_{v1})(1 - \tilde{f}_{v2})}{\chi}. \tag{8}$$

Now $\widetilde{S} \geqslant 0$. Nevertheless, if both $\tilde{\nu}$ and S are equal to zero, then $\widetilde{S}$ is still zero. An efficient mean for vanishing numerical problems is to take $\max(\chi, 10^{-4})$ instead of χ. Spalart also suggested to take $c_{v2} = 5$.

Modified f_{v2} function remains positive along the wall. Modified function f_{v3} differs notably from 1 in the vicinity of walls. This results in a modification of the natural laminar-turbulent transition of the model.

2.3. Possible extensions to compressible flows

A natural way to take into account some possible compressibility effects is to use $\bar{\rho}\tilde{\nu}$ instead of $\tilde{\nu}$ as working variable: Another solution has been proposed by Catris and Aupoix [8] by modifying the diffusion laws in the turbulence model. Catris suggests to advect $\bar{\rho}\tilde{\nu}$ and to diffuse $\sqrt{\bar{\rho}}\tilde{\nu}$. Nevertheless, this strategy complicates the numerical implementation. We preferred another form of (1) which can also be found in [7]:

$$\frac{D\bar{\rho}\tilde{\nu}}{Dt} = c_{b1}\widetilde{S}\bar{\rho}\tilde{\nu} + \frac{1}{\sigma}\big(\nabla.(\mu + \bar{\rho}\tilde{\nu})\nabla\tilde{\nu} + c_{b2}\nabla\tilde{\nu}\nabla\bar{\rho}\tilde{\nu}\big) - \bar{\rho}c_{w1}f_w\left(\frac{\tilde{\nu}}{d}\right)^2. \tag{9}$$

This formulation needs the calculation of $\nabla\bar{\rho}\tilde{\nu}$ which appears only in the source term.

3. Numerical method

3.1. Integral form of governing equations

The governing equations are the Navier–Stokes ones. For turbulent flows, a Reynolds averaged form is used, where the conservative variables are mass averaged and represent the mean flow contributions. Considering a finite volume Ω, its surface $\partial\Omega$ with an exterior normal $\vec{n}$, the integration of the RANS equations leads to the following integral form:

$$\frac{\partial}{\partial t}\int_{\Omega} \vec{W}\,\mathrm{d}\Omega + \oint_{\partial\Omega} \big[\overline{\overline{\mathcal{F}}}_c[\vec{W}] - \overline{\overline{\mathcal{F}}}_d[\vec{W}, \nabla\vec{W}]\big].\vec{n}\,\mathrm{d}\Sigma = \int_{\Omega} \vec{T}[\vec{W}, \nabla\vec{W}]\,\mathrm{d}\Omega \tag{10}$$

with

$$\begin{cases} \vec{W} = {}^t(\bar{\rho}, \bar{\rho}\vec{V}, \rho E) + {}^t(\bar{\rho}\tilde{\nu}), \\ \overline{\overline{\mathcal{F}}}_c = {}^t(\rho\vec{V}, \rho(\vec{V}\otimes\vec{V}) + P\bar{\bar{1}}, \rho E\vec{V} + P\vec{V}) + {}^t(\bar{\rho}\tilde{\nu}.\vec{V}), \\ \overline{\overline{\mathcal{F}}}_d = {}^t\big(0, \bar{\bar{\tau}} + \bar{\bar{\tau}}_R, (\bar{\bar{\tau}} + \bar{\bar{\tau}}_R).\vec{V} - (\vec{q} + \vec{q}_t)\big) \\ \qquad\quad + {}^t\big(-\frac{1}{\sigma}(\mu + \bar{\rho}\tilde{\nu})\nabla\tilde{\nu}\big), \\ \vec{T} = {}^t(0) + {}^t\big(c_{b1}\widetilde{S}\bar{\rho}\tilde{\nu} + \frac{c_{b2}}{\sigma}\nabla\bar{\rho}\tilde{\nu}\nabla\tilde{\nu} - \bar{\rho}c_w f_w\big(\frac{\tilde{\nu}}{d}\big)^2\big). \end{cases} \tag{11}$$

The above system is formulated in an absolute frame. Turbulence contribution is reduced to the Reynolds tensor $\bar{\bar{\tau}}_R$ and to the turbulent heat transfert $\vec{q}_t$. The first source term in (11) is written equal to 0 to recall that the turbulence equation is decoupled from the RANS equations. This strategy makes the numerical implementation easier and reduces CPU cost per iteration since the costly construction and inversion of a (6×6) matrix for each grid point is not required. Assuming the air as an ideal gas, the state equation relates the static pressure P to the conservative variables:

$$P = (\gamma - 1)\left(\rho E - \frac{(\rho\vec{V})^2}{2\rho}\right). \tag{12}$$

For a Newtonian fluid, shear stresses are related to mean velocity gradients. Apparent turbulent stresses are also related to mean velocity gradients, using Boussinesq's assumption:

$$\bar{\bar{\tau}} + \bar{\bar{\tau}}_R = (\mu + \mu_t)\left[-\frac{2}{3}\big(\operatorname{div}\vec{V}\big)\bar{\bar{1}} + \big(\overline{\overline{\operatorname{grad}}}\vec{V} + {}^t\overline{\overline{\operatorname{grad}}}\vec{V}\big)\right]. \tag{13}$$

For the dependance of the laminar viscosity on temperature, Sutherland's law is used:

$$\mu(T) = \mu_0\left(\frac{T}{T_0}\right)^{3/2}.\frac{T_0 + 110.4}{T + 110.4} \tag{14}$$

with $T_0 = 273.16$ K and $\mu_0 = 1.711.10^{-5}\,\mathrm{kg\,m^{-1}\,s^{-1}}$.

3.2. Numerical algorithm

The numerical method, implemented in the computer solver FLU3M is based on the finite volume approach (10) and on a cell centered discretization. Computations are realized by block, each block being divided in hexaedral cells. Time discretization is based on second-order accurate Gear's formulation of the fully implicit scheme:

$$\overline{\Omega}_{ijk}\frac{\frac{3}{2}\vec{W}^{n+1}_{ijk} - 2\vec{W}^{n}_{ijk} + \frac{1}{2}\vec{W}^{n-1}_{ijk}}{\Delta t} + \sum_{l=1}^{6}(\vec{Fc} - \vec{Fd})^{n+1}_{ijk,l} = 0 \tag{15}$$

where ijk are the grid indices, l one of the six interfaces of the hexaedral rigid cell Ω_{ijk} and $(\vec{Fc} - \vec{Fd})_{ijk,l}^{n+1}$ denotes the fluxes budget through interface l. Subscript n refers to the time evaluation. The implicit formulation results in inversion of a large sparse matrix system. The LU [17] factorization simplifies the inversion of the latter implicit system. Roe's [23] flux difference splitting is employed to obtain advective fluxes at cell interface. MUSCL [27] approach extends the spatial accuracy to the second order and is combined with minmod or Van Albada's limiter. All viscous terms are centrally differenced. Further details of the numerical method for RANS equations can be found in Ref. [9,21]. Concerning the turbulent variable, special care has to be taken to ensure a non-negative eddy viscosity ($\tilde{\nu} \geqslant 0$) at all grid points and at all time steps. This can be achieved by a proper linearization of the advective, diffusive and source terms. The linearization of the turbulence equation follows Spalart's approach [25]. They construct, following Baldwin and Barth analysis [3], an implicit operator such that a positive turbulence field is obtained for all transient solution states.

3.3. Boundary conditions

In this cell centered discretization, every boundary condition is imposed by ensuring adequate fluxes at boundary interfaces. Inviscid boundary conditions are based on characteristics theory [28].

Numerical implementation of diffusive wall boundary conditions is a subject which, despite its considerable practical importance, receives little attention in the literature. The numerical solid wall boundary condition for cell-centered finite volume discretization procedures is presented. The viscous and diffusive flux computation needs the knowledge of interface primitive states and gradients. These gradients are defined by the average over an adequate control volume $\overline{\Omega}_{ijk}$ using Green formulae:

$$(\nabla \Phi)_{ijk} \approx \frac{1}{\overline{\Omega}_{ijk}} \iint_{\partial \Omega_{ijk}} \Phi . \vec{n}_{\text{ext}} \, \mathrm{d}S. \tag{16}$$

Ben Khelil [5] has tested two approximations. The first one uses staggered cells in order to evaluate the gradients at cell interface. The second one, more simple, computes the cell gradient at each cell center and affects an averaged value at the interface. The use of a centered control volume method simplifies considerably the treatment of boundary conditions. Nevertheless, the use of a centered volume leads theoretically to parasite oscillations due to an uncoupling between even and odd points. In practice, this uncoupling has no consequence for our high speed flow configurations. However, parasite oscillations can appear when diffusive terms become dominating and more precisely, in the vicinity of walls. Turbulent variables are particularly sensitive to this problem. Consequently, wall interfaces require some specific treatments.

- Treatment of the turbulent variable

We have seen that one of the numerical properties of SA model is that $\tilde{\nu}$ maintains its log-layer behaviour ($\tilde{\nu} = \kappa u_\tau y$) until the wall. We propose a very simple but efficient mean for calculating the gradient in the fictitious cell "0" (see Fig. 1) which consists to extrapolate the gradient associated at the real cells '1', '2' and '3':

$$\nabla_0 = \alpha_1 \nabla_1 + \alpha_2 \nabla_2 + \alpha_3 \nabla_3. \tag{17}$$

The extrapolation coefficients do not depends on the discretization cell geometry. These latter are chosen in function of the desired degree of precision (see Table 1).

- Treatment of velocity gradient

The above technique for the turbulent variable can be used for the calculation of velocity gradient in fictitious cells if the viscous sublayer mesh is sufficiently refined. Fictitious values influence directly slopes in wall real cells due to the MUSCL approach. The linear velocity profile holds classically for $y^+ \leqslant 3$ [2]. Therefore, the second order accuracy extrapolation is not recommanded for the calculation of the velocity gradients in fictitious cells. Péchier [21] proposed another technique giving gradients in fictitious cells. The first real cell '1' is divided in two equal cells (Fig. 1). Gradients are evaluated in the nearest half cell from the wall (subscript $1, 1/2$) with the following expression:

$$(\nabla \Phi)_{1,1/2} \approx \frac{1}{\overline{\Omega}_{1,1/2}} \big((\Phi \vec{S})_{0,1/2} + (\Phi \vec{S})_{1,1/2} \big). \tag{18}$$

Table 1

	α_1	α_2	α_3
Order 0	1	0	0
Order 1	2	−1	0
Order 2	3	−3	1

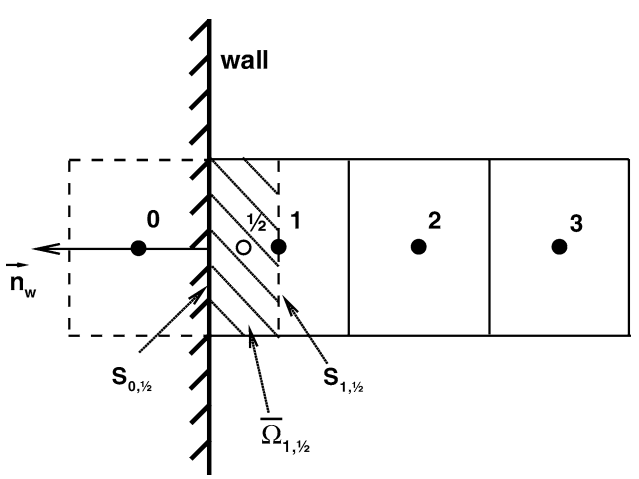

Fig. 1. Wall real and fictitious cells.

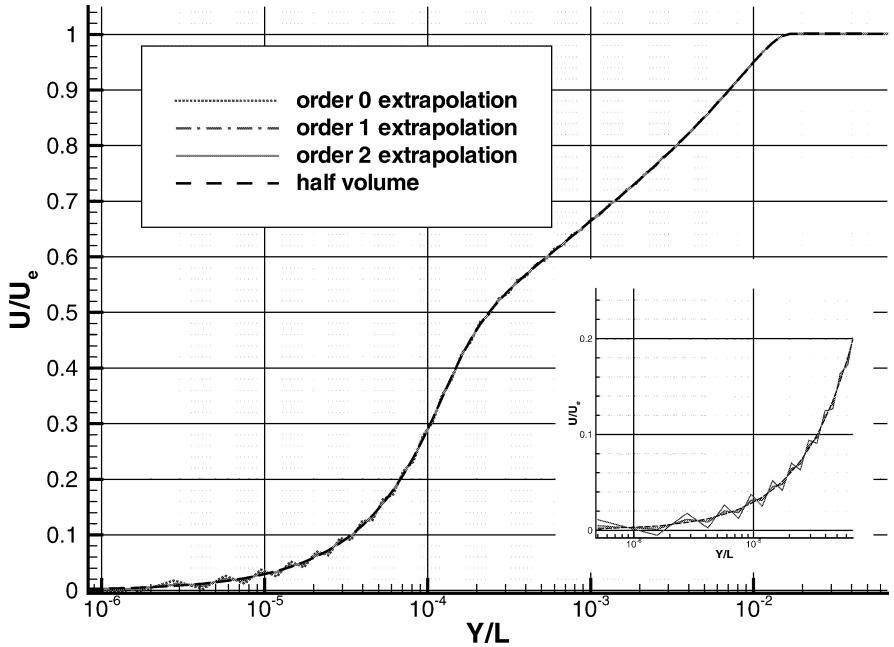

Fig. 2. Influence of gradient calculation in fictitious cells.

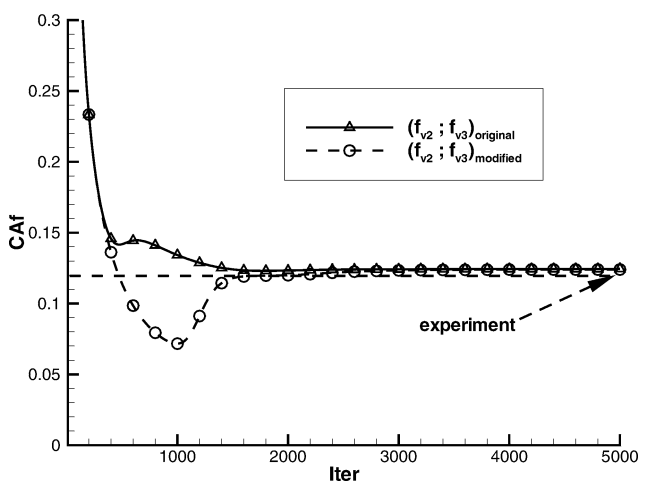

Fig. 3. Convergence history.

Then gradients in fictitious cells are extrapolated from:

$$(\nabla\Phi)_0 \approx 4(\nabla\Phi)_{1,1/2} - 3(\nabla\Phi)_1. \tag{19}$$

Fig. 2 presents a typical velocity profile of a flat plate in supersonic free-stream conditions; this profile corresponds to cell-centered values. A comparison of different computational techniques for gradient calculation is given. A zero order extrapolation results inevitably in parasite oscillations due to an uncoupling between even and odd points. Nevertheless, one can notice no oscillation when using the half volume technique or second order extrapolation. Finally the second order gradient extrapolation for turbulent variables appears to be a suitable compromise between accuracy and robustness. Numerical implementation of the above technique is immediate. The half volume technique is used for calculation of velocity gradients in fictitious cells.

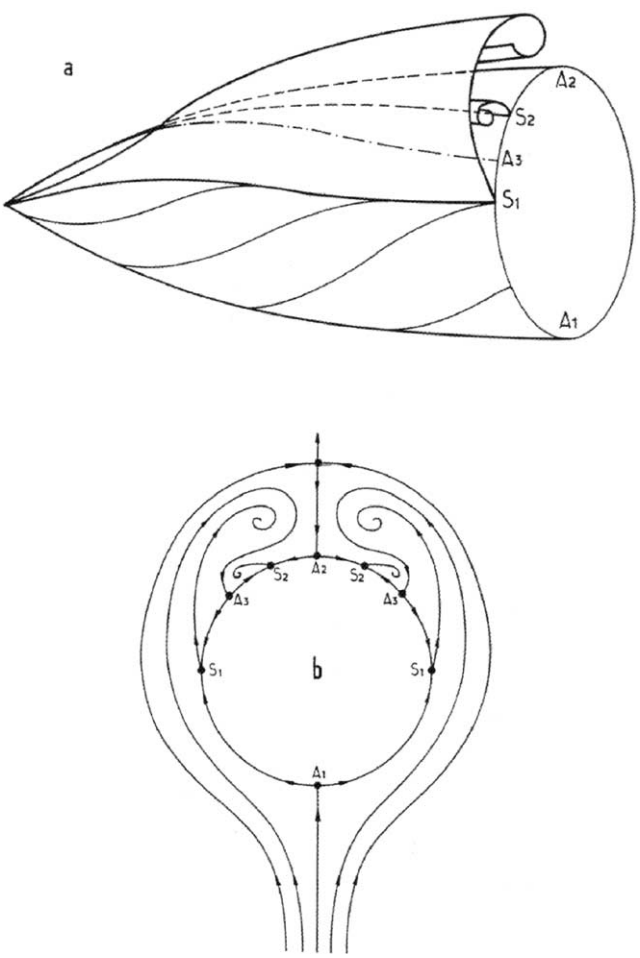

Fig. 4. Sketch of the flowfield $\alpha = 10$ deg (issued from Ref. [20]).

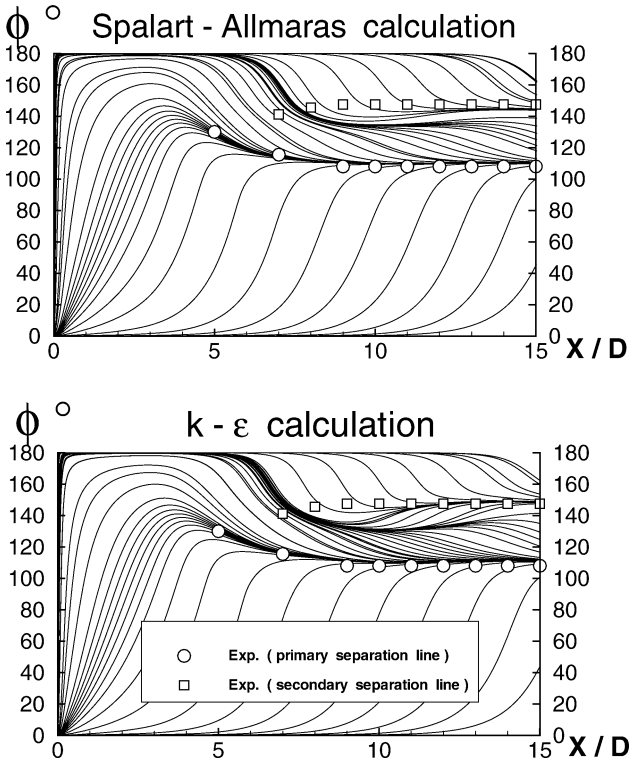

Fig. 5. Skin friction contours and separation lines.

4. Results-discussion

4.1. External flows

SA model implemented in FLU3M has been validated with various conventional configurations as a part of the SIAM (Simulation Industrielle de l'Aérodynamique des Missiles) program. Two simple but representative test cases have been chosen for generic configurations at Mach 2 and moderate angle of attack: a simple circular body and a body-tail configuration.

4.1.1. Ogive-cylinder $\alpha = 0$

A basic study of the influence of f_v functions is conducted for $\alpha = 0$ deg. The flow is turbulent (forced transition near the body nose) and Reynolds number based on the diameter is equal to $1.2\,10^6$. Fig. 3 presents a typical convergence history of the friction drag coefficient (most restricting criterion) together with the experimental value. Modified functions (f_{v2}, f_{v3}) shifts laminar-turbulent transition backward but do not modify the converged value of the normal force coefficient. Moreover, one can notice a slight difference of speed convergence; the steady state is reached after only 1700 iterations with original f_v functions while 3000 iterations are necessary to obtain the same value with modified f_v functions. Both calculations have been performed with a CFL number equals to 50.

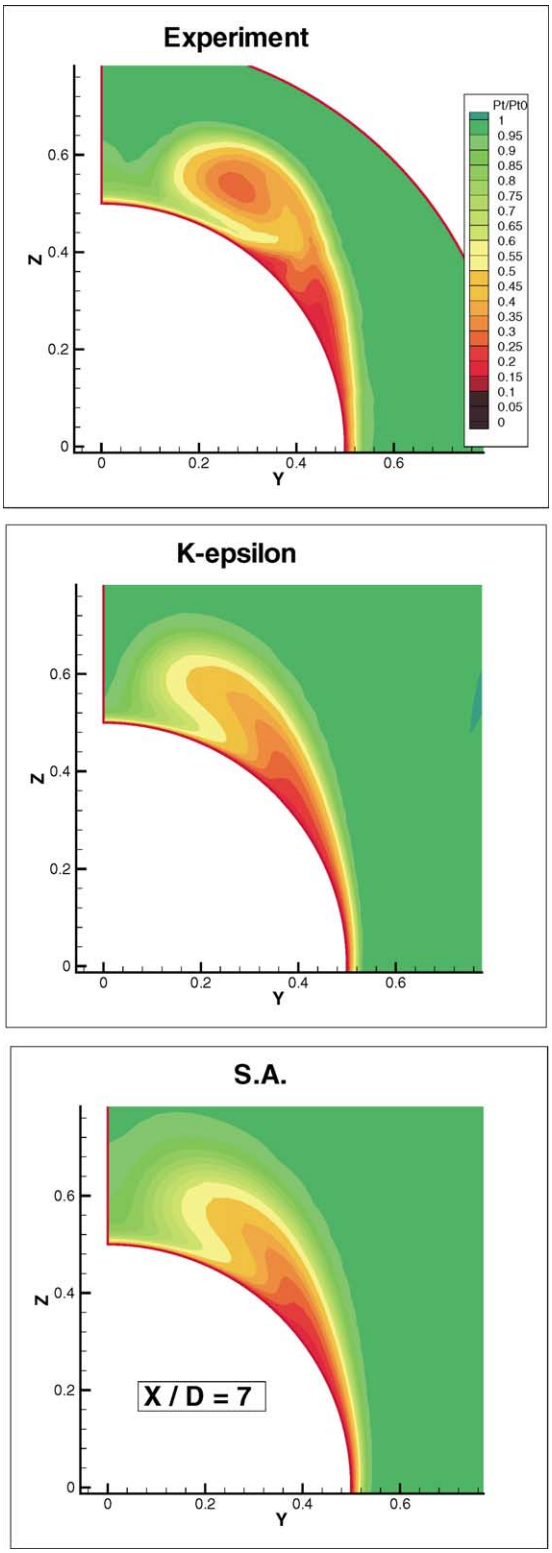

Fig. 6. Total pressure (p_i/p_{i0}) contours in the cross section $X/D = 7$ at $\alpha = 10$ deg.

4.1.2. Ogive-cylinder $\alpha = 10$

A detailed experimental study of an ogive cylinder (oil flow visualisations, flowfield measurements, pressure distributions, boundary layer profiles, skin friction values)

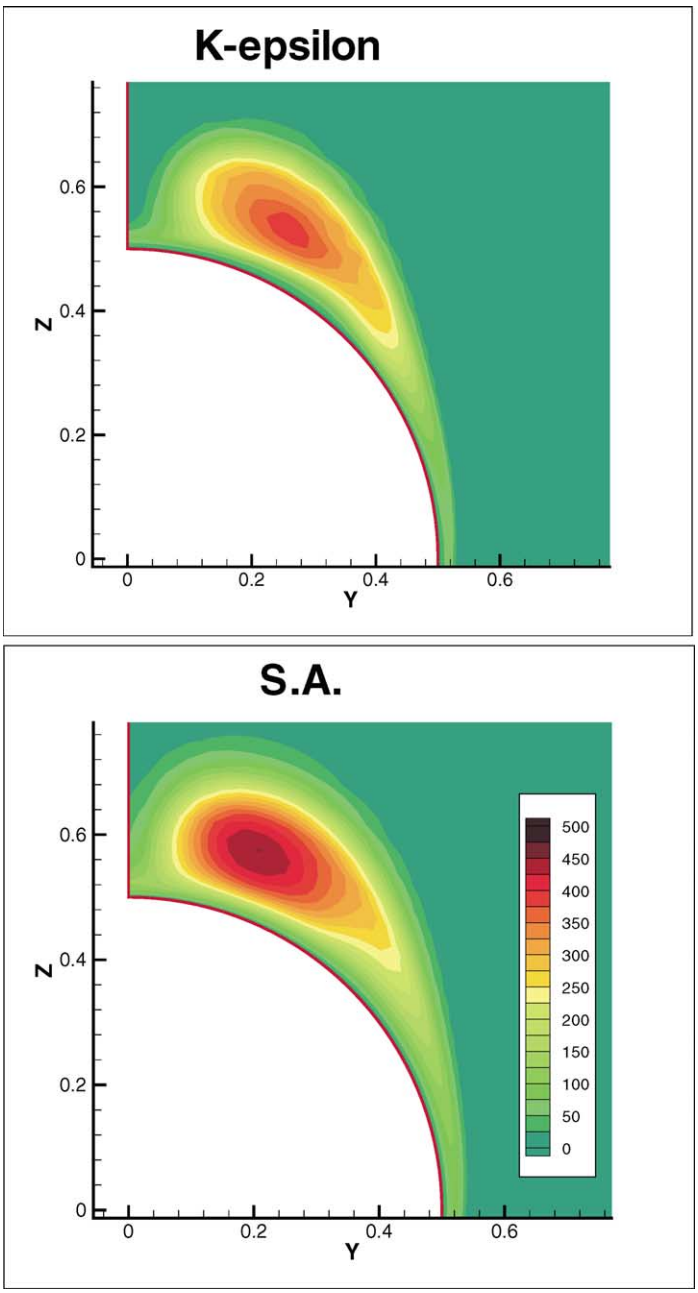

Fig. 7. Eddy viscosity field.

has been carried out at ONERA wind tunnels at Mach 2, particularly at 10 deg of incidence. The flow structure is classical, including a primary vortex and a secondary one (Fig. 4), but the major interest of this test case is that the intensity of the vortex flow is highly sensitive to the laminar or turbulent nature of the boundary-layers. Indeed, within the framework of a GARTEUR group (AG24), this results were already used to test and compare a lot of turbulence models and codes. Two Reynolds numbers have been under consideration. First experiments [20] are carried out with a 'transitional' Reynolds number ReyD = 0.16 millions (based on the diameter of the cylinder). This allowed to switch from laminar to turbulent boundary layer when the transition was free or triggered on the body apex (the nature of the boundary have was controlled by acenaphtene coating visualisation). To be sure that the flow is 'fully turbulent' and also to complete the database, a lot of experiments with a Reynolds number (ReyD = 1.2 millions) were conducted in a second step [14].

Freestream conditions are Mach = 2 and $\alpha = 10°$. Laminar calculations are performed with ReyD = 0.16 millions and ReyD = 1.2 millions for all other turbulent calculations.

The grid, has about 400 000 points (61 in the axial direction, 85 in the radial direction, 73 in circumferential direction with $\Delta\Phi = 2.5$ deg). Moreover, a normal size cell

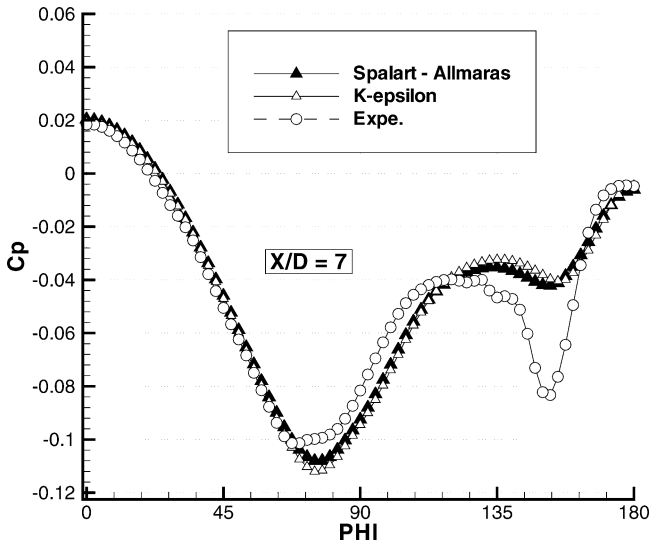

Fig. 8. Wall pressure coefficient (*Cp*).

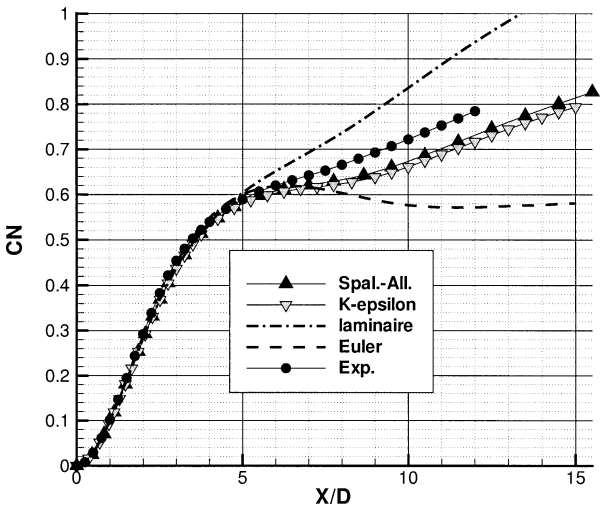

Fig. 9. Comparison of the normal force coefficient (*CN*).

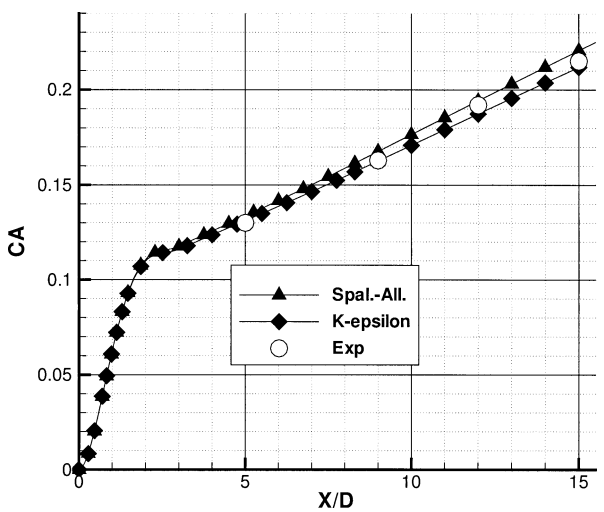

Fig. 10. Total axial force coefficient.

in axial direction (equal to 2.5 10–6 D) leading to $Y^+ < 1$ is assumed around the whole body (checked with calculations at $\alpha = 0$).

The numerical validation is completed with a K-epsilon model computation (Jones and Launder [18]).

Computed skin friction lines are presented on Fig. 5 (developed view). Experimental location of primary and secondary separation lines are obtained from oil flow visualisations. One can notice a good position of the primary separation line is observed with both models, the second separation line is quite visible.

At station $X/D = 7$ the main vortex on upper side of the body shown by total pressure contours of Fig. 6, is already developed for this angle of attack. The secondary vortex is embedded in the boundary layer and cannot therefore be clearly seen. It is wellknown that computational results are very sensitive to viscous effects (laminar/turbulent) and to turbulence modelling [14]. Moreover SA and K-epsilon give very close results for total pressure and eddy-viscosity (Fig. 7).

Under the main vortical in leeward side ($\phi = 140$ deg) a suction peak is found on the pressure distributions (Fig. 8). This peak is linked to the high intensity of vortex primary structure and to wall proximity. K-epsilon, and SA models agree with the experiment, except near this peak due to an overprediction of the eddy viscosity.

The cumulated normal force coefficient obtained by integration of pressure distributions along the body is presented Fig. 9. Euler and laminar calculations are also presented. The differences are clearly related to the vortical lift and eddy viscosity: no vortical lift for Euler calculations, under estimation of vortical lift for K-epsilon and SA calculations.

In spite of slight differences in normal force coefficient (*CN*), both models give the same axial force coefficients (pressure + skin friction) and compare well with the experimental results as can be seen on Fig. 10.

4.1.3. Body-tail configuration

This second test case was considered in order to get an insight into the effect of vortices on the overall aerodynamics of a body-fin configuration, and more precisely on the induced rolling moment. The results presented hereafter were obtained at Mach 2 and for a non-symmetric roll angle of 22.5°. Euler and Spalart–Allmaras solutions are compared to experiments. Fig. 11 shows the forebody vortices acting on the fins.

The prediction of normal force (Fig. 12) is very good for the Spalart–Allmaras computation, but not so bad for the inviscid one. This is quite surprising, and can be explained by the fact that with the inviscid solution the body lift is underestimated (as seen above), whereas the fin lift is overestimated (no or very small effect of the vortices). On the other hand, an accurate estimation of the rolling moment is only obtained by taking into account the viscous effects

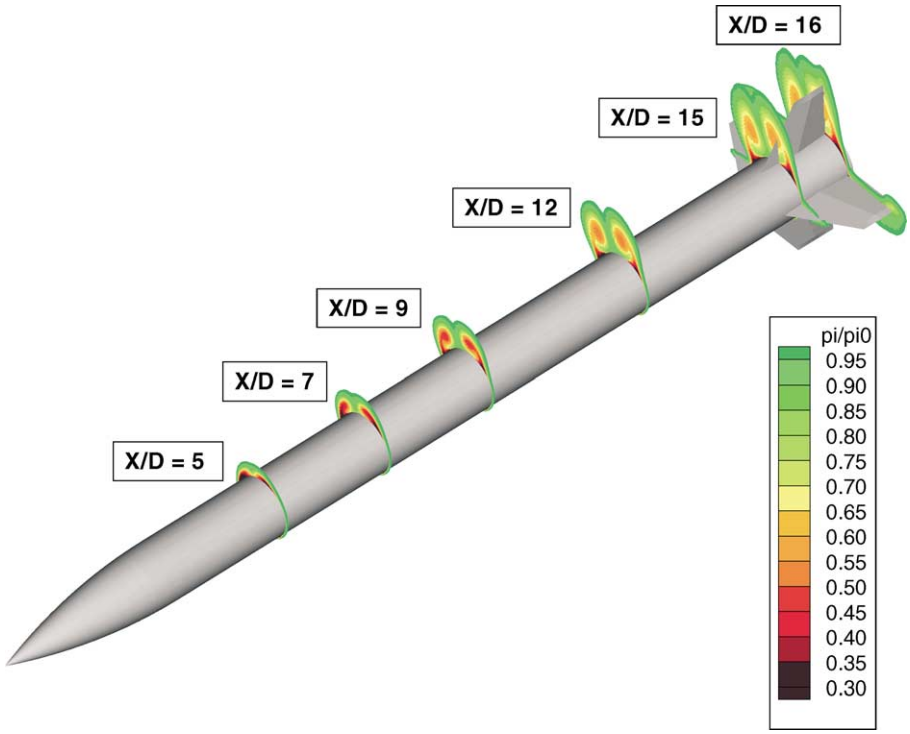

Fig. 11. Total pressure contours.

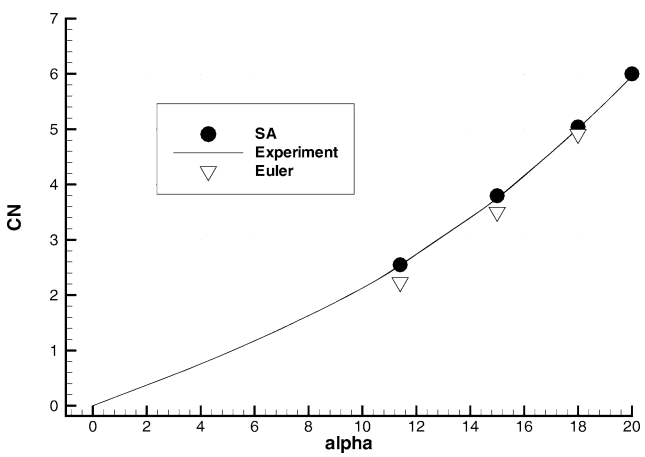

Fig. 12. Normal force coefficient.

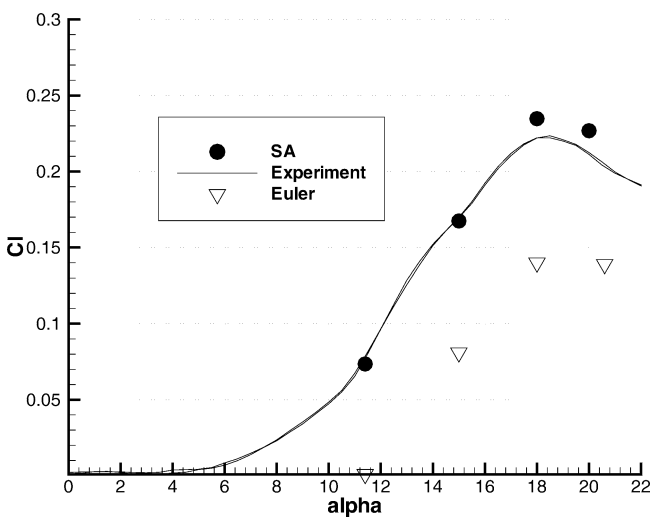

Fig. 13. Polar in roll fuselage + wing.

(Spalart–Allmaras model on Fig. 13) because it is highly dependent on the individual contribution of each fin.

Generic configurations have been studied for supersonic flow and moderate angles of attack: a body alone and a body-tail. For the body alone a detailed study was performed at 10° of incidence. None of the models is really satisfactory: Spalart–Allmaras and K-epsilon (Jones–Launder) give very close results between one another but slightly overestimate the eddy viscosity. The *CN* induced by the vortical flow developed on leeward side is very sensitive to viscous effects (laminar/turbulent) and to the turbulence model. However, for configurations with rear tails, body vortical flow have no tangible effect on the global longitudinal characteristics (*CN*) as showed by the good agreement obtained with inviscid calculations. Taking into account the vortical body is important to predict correctly the rolling moment. This was done with SA model.

4.2. Internal flows

In the frame of 'JAPHAR' project, focused on scramjet technologies and involving DLR and ONERA [19], an internal compression inlet was designed to match the requirements of a mixed-combustion engine between Mach number 4 and 8 [15].

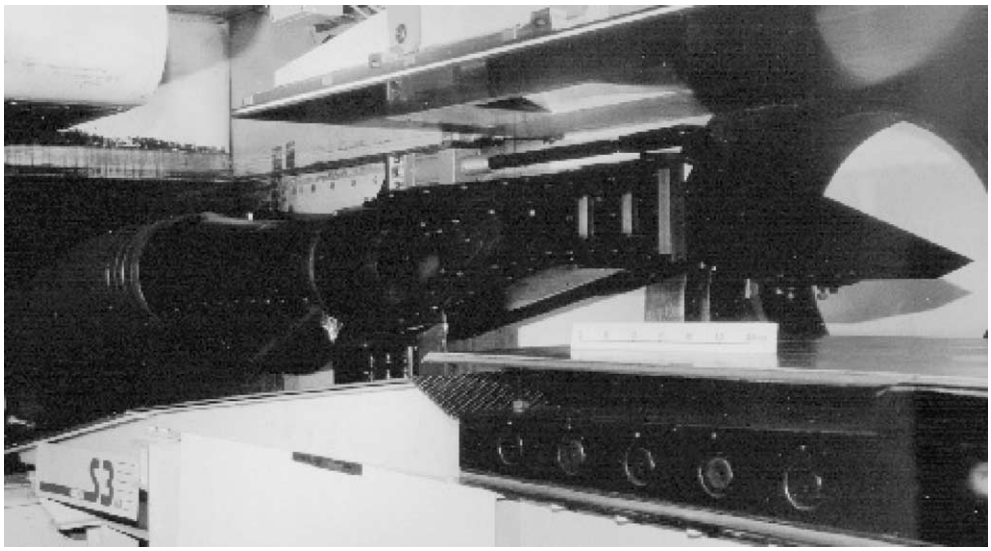

Fig. 14. Isolated inlet in S3MA wind tunnel.

This inlet is supposed to be operated with fixed geometry on a small scale flight test vehicle propelled by a scramjet engine burning hydrogen as a fuel. The air flow is decelerated trough a series of ramps prior to the combustion chamber and, since the compression process is fully internal, four boundary layer bleeds are positioned upstream the inlet throat in order to minimise corner flow developments and shock induced boundary layer separations. A contraction ratio around 4 is chosen to decelerate the air flow sufficiently at high Mach number while keeping stabilised flow conditions inside the inlet at the lowest bound of the flight range.

The inlet design is influenced to a great extent by the design of the scramjet engine itself. Two struts levels are indeed installed in the combustion chamber for an efficient fuel injection and mixing in the air. Furthermore, since ignition delays are quite high in supersonic flows, the inlet diffuser must act as scramjet chamber: hence, the struts are positioned in its upstream part, where only a small amount of divergence is allowed to minimise losses associated with supersonic combustion. All these features give the inlet highly three-dimensional characteristics and make its numerical simulation a real challenge.

4.2.1. S3MA tests

A scale 0.4 model of the isolated inlet was tested in S3MA wind tunnel between Mach number 3.5 and 5.5, which roughly corresponds to flight conditions in the range Mach 4 to 7 due to the forebody precompression effect. The purpose of these tests was to select a candidate inlet for JAPHAR vehicle but also to provide experimental data on a complex configuration for the validation of the FLU3M code. Fig. 14 shows the isolated inlet mounted upside down in S3MA half wind tunnel. The inlet is connected to a mass flow meter and throttled by mean of a rotating butterfly valve

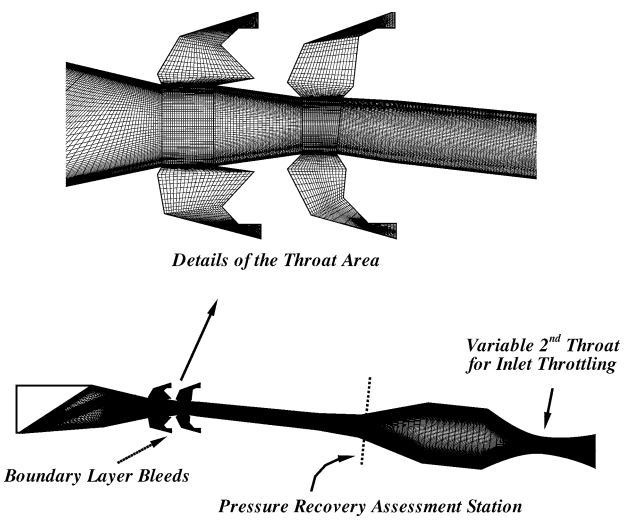

Fig. 15. Grid symmetry plane.

in order to obtain its characteristic curve (pressure recovery versus mass flow).

35 static pressure taps are positioned on the inlet ramps and sidewalls. The instrumentation includes a 35 pitot probe rake located downstream the second struts level in the station selected for pressure recovery assessment. Mach 3.5 test conditions have finally been chosen for the validation; it makes indeed sense to simulate the entire characteristic curve of the inlet in this case which corresponds to the operation of a classical ramjet, with subsonic combustion. Test conditions are given below: $M_0 = 3,49$, $P_i = 3,71$ bar and $T_i = 344$ K, leading to a unit Reynolds number of $17.4\,10^6\ \mathrm{m}^{-1}$.

4.2.2. Numerical approach

A 28 domain grid of 2.9 million points was built to simulate the flow in only half the inlet since there is a vertical symmetry plane. The grid is clustered near the walls:

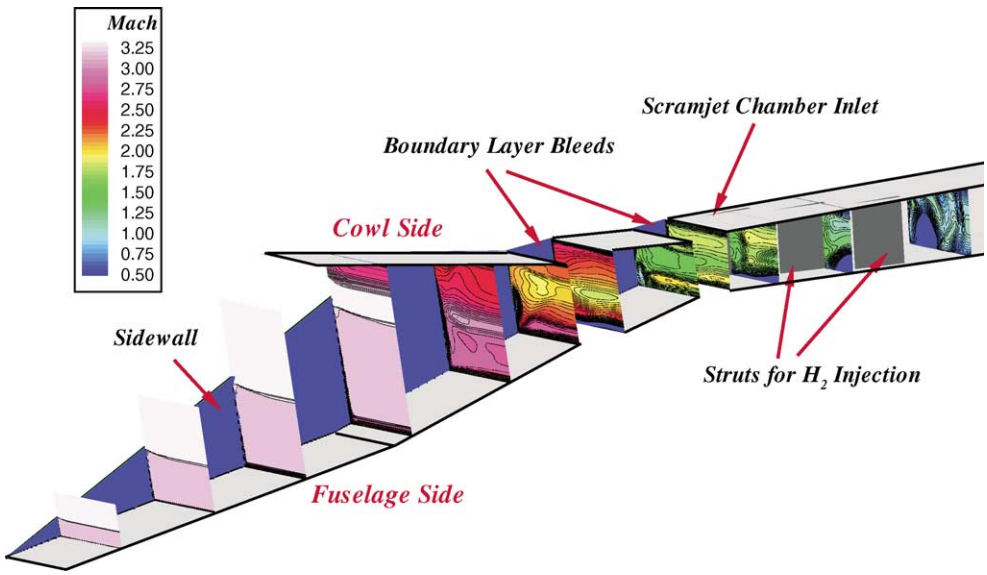

Fig. 16. Iso-Mach contours.

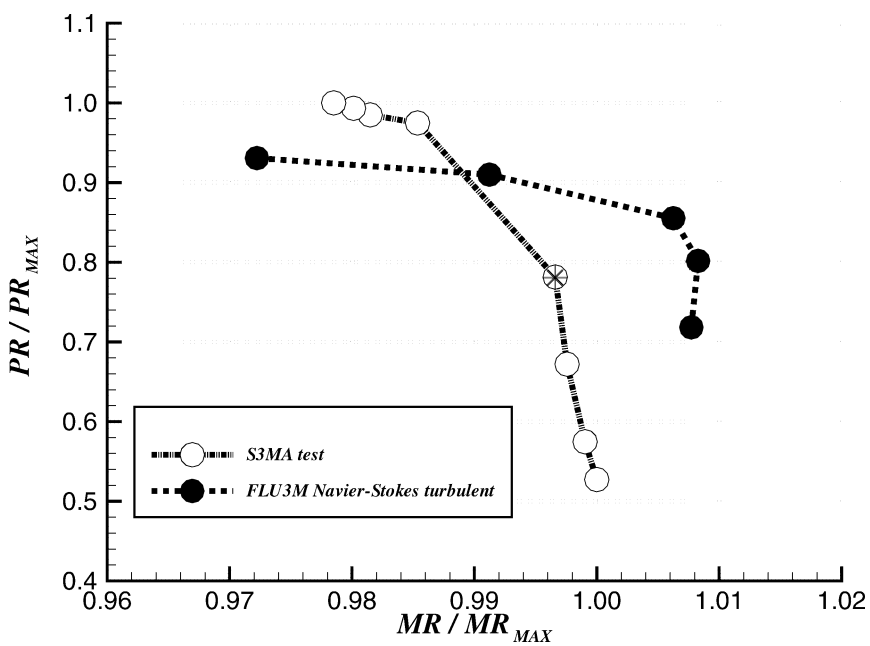

Fig. 17. Characteristic curves.

30 points are distributed along the empirically assumed boundary layer height according to a tangent hyperbolic law, except in the boundary layer bleeds to avoid the capture of undesirable vortices likely to make the solution unstable, and around the struts, considered here as mere obstacles or shock generators. The height of the first cell is within 5–10 μm depending on the longitudinal position along the inlet in order to insure y^+ wall values around 1. The mesh size has been limited purposely, keeping in mind the calculation time (see later on). 91 points are distributed along the duct height and 60 points in spanwise direction. Three external domains allow to take into account supersonic inflow boundary conditions and flow spillage. Fig. 15 gives the overall view of the mesh corresponding to the symmetry plane of the inlet together with some details of the throat area.

RANS calculations have been performed using Spalart–Allmaras turbulence model fully described above, with a CFL number equal to 3 and local time-stepping since only the steady state flow is studied here. Supersonic inflow boundary conditions are imposed wherever they are required to simulate the external flow ahead of the inlet and inactive conditions are imposed at the exit stations of the boundary layer bleeds and of the 2nd throat. No-slip adiabatic boundary conditions are imposed at the walls except on the struts where a slipping condition is imposed. In order to obtain a fully converged solution for the first operating point of the

inlet, starting from a uniform state at Mach 3.5, 35 000 iterations are necessary, which means roughly 45 h CPU on ONERA NEC SX-5 supercomputer. The other points only require 25 000 iterations to reach convergence, and are obtained step by step, closing progressively the 2nd throat.

4.2.3. Results and discussion

The three-dimensionality of the internal flowfield is highlighted by Fig. 16 showing several iso-Mach slices down to the first struts level. In this example, the transition between supersonic and subsonic flow is achieved through a complex system of shock trains located around the upstream struts, which results in large flow distortions in the chamber.

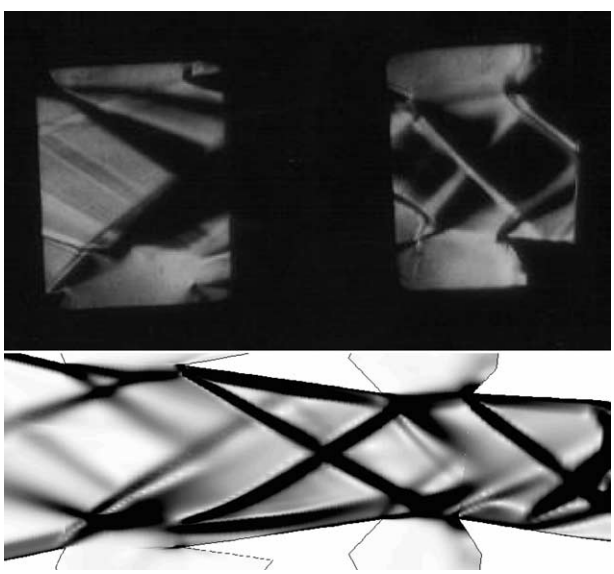

Fig. 18. Shadowgraph: S3MA test (up)/FLU3M SA computation (bottom).

The experimental and numerical characteristic curves are compared on Fig. 17. More precisely, the Mass flow Ratio (MR) is a ratio of the engine mass flow (mass flow at the end of the diffuser) to the theoretical mass flow which could be capted through the projected front area of the inlet. The maximum MR is assessed precisely which means that the spillage is correctly taken into account as well as bleed mass flow.

On the other hand, the agreement is much poorer on PR (underestimation by 7%) which is not so surprising if one considers the complex flow pattern with numerous shock-boundary layer and shock-shear layers interactions. Indeed, the turbulence model experiences difficulties to assess the right position and extent of the separated flow regions, particularly around the inlet throat and in the diffuser.

A close examination of the flowfield reveals that the shear layers originating in the trailing edges of the upstream ramps are subject to strong shock interactions at the level of the first bleeds. This results mainly in a large area of separated flow just above the lower bleed (see Schlieren picture on Fig. 18), the extent of which being very difficult to predict numerically, and in a complex shock-expansion flow pattern downstream the interaction region. A look at the numerical Schlieren picture of Fig. 18, close to the experimental point (see points denoted by a star on Fig. 17), indicates nevertheless that the flow pattern is rather well reproduced in the visualised region.

Differences in wall pressures are observed on the internal ramps (see around $X = -840$ mm on Fig. 19), particularly at fuselage side (lower side on Schlieren pictures), which is due to a bad prediction of the shear layer reattachment downstream the bleed. This certainly effects downstream bleeds efficiency and could explain to some extent the poor

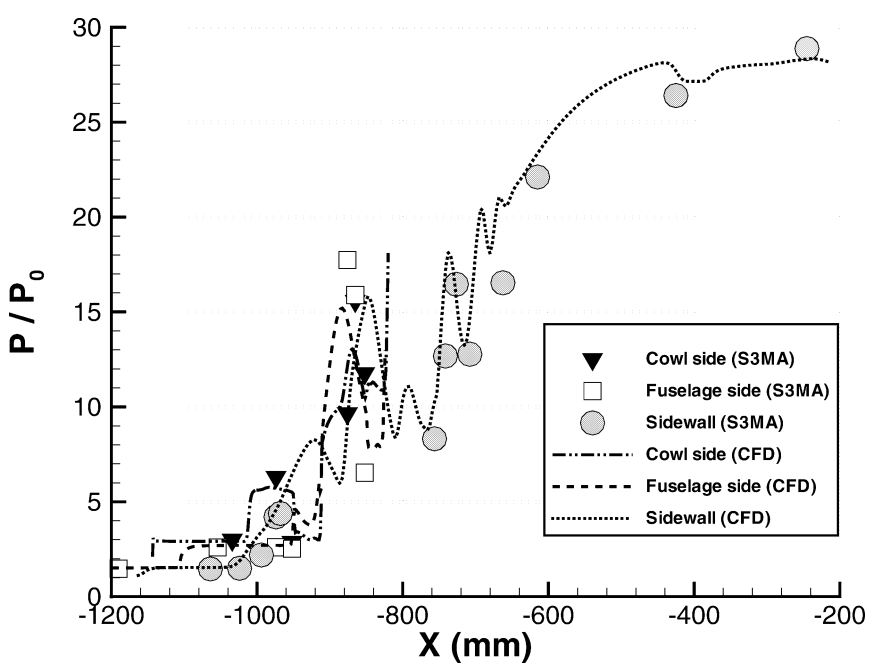

Fig. 19. Pressure distribution.

agreement between numerical and experimental pressure recovery in critical regime.

In spite of these reserves, the comparison between numerical and experimental results remains quite acceptable, particularly if one considers the sidewall pressure distributions resulting from a very complex flow field in the scramjet chamber.

5. Conclusion

Spalart–Allmaras turbulence model has been developped and designed for subsonic flow around airfoils. Extension to subsonic and to transonic flows around aircraft configurations using its original form has been already achieved by several authors.

An extension of its formulation to compressible flows and its application to three-dimensionnal supersonic complex configurations have been achieved. Special care has to be taken concerning the definition of the model damping functions and the discretization of viscous gradients near boundaries in order to get a correct behaviour of the numerical boundary layers. The accuracy and the usefulness of this model for supersonic flows is demonstrated. Simulations over a cruciform missile showed the ability to capturing ogive leeward side vortices which have a major influence for the assesment of external flows. The ability to handle complex configurations is pointed out through the validation of a numerical simulation of a three-dimensionnal supersonic inlet including corners, boundary layer bleeds and struts.

Future work will concern the extension of the domain of application to unsteady flows.

Acknowledgements

It is the authors' pleasure to acknowledge B. Aupoix for fruitful discussions.

References

[1] M. Amato, G. Iaccarino, Filtering algebraic turbulence models for supersonic high-incidence missile flows, in: RTO AVT Symp. on Missile Aerodynamics, Sorrento, Italy, 1998.
[2] B. Aupoix, Introduction to Turbulence Modeling for Compressible Flows, von Karman, Lecture Series, 2000.
[3] B. Baldwin, T.J. Barth, A one-equation turbulence transport model for high Reynolds number wall-bounded flows, AIAA Paper 91-0610, 1991.
[4] B.S. Baldwin, H. Lomax, Thin layer approximation of algebraic model for separated flows, AIAA Paper 78-0257, 1978.
[5] S. Ben Khelil, Simulation numérique d'écoulements turbulents autour de configurations complexes. Application au roulis induit des missiles, PhD thesis, Université de Paris 13, 1998.
[6] S. Ben Khelil, Ph. Guillen, M. Lazareff, R.G. Lacau, Numerical simulation of roll induced moment of cruciform tactical missiles, Aerospace Science and Technology 5 (2001) 109–124.
[7] S. Catris, Etude de contraintes et qualification de modèles à viscosité turbulente, PhD thesis, SupAéro, 1999.
[8] S. Catris, B. Aupoix, Density corrections for turbulence models, Aerospace Science and Technology 4 (2000) 1–11.
[9] D. Darracq, Etude numérique des interactions choc/choc et choc/couche limite turbulente en régime hypersonique, PhD thesis, Université de Poitiers, 1995.
[10] S. Deck, Ph. Guillen, Numerical simulation of side loads in an ideal truncated nozzle, AIAA J. Propulsion Power, to appear.
[11] S. Deck, R. Hallard, Simulations numériques des écoulements décollés dans les tuyères, in: 37eme colloque d'Aérodynamique Appliquée, Aérodynamique et Propulsion des véhicules à grande vitesse, Arcachon, France, 2001, pp. 103–111.
[12] D. Degani, L.B. Schiff, Computation of supersonic viscous flows around pointed bodies at large incidence, AIAA Paper 83-0034, 1983.
[13] H. Deniau, Calcul d'écoulements supersoniques pou résolution des équations de Navier–Stokes parabolisées: Modélisation de la Turbulence. Traitement des poches subsoniques, PhD thesis, ENSAE, 1996.
[14] P. d'Espiney, P. Champigny, D. Baudin, J.A. Pilon, Couche limite autour d'un fuselage en incidence en écoulement supersonique, in: RTO AVT Symp. on Missile Aerodynamics, Sorrento, Italy, 1998.
[15] P. Duveau, H. Esch, K. Triesch, Inlet design for JAPHAR flight test vehicle, in: XV ISABE Congress, Bangalore, India, 2001.
[16] C. Gacherieu, C. Weber, Assesment of algebraic and one-equation turbulence models for transonic turbulent flow around a full aircraft configuration, AIAA Paper 98-32457, 1998.
[17] A. Jameson, Young, Lower-upper implicit scheme with multiple grids for the Euler equations, AIAA J. 25 (7) (1987).
[18] W.P. Jones, B.E. Launder, The prediction of laminarization with a 2-equation model of turbulence, Internat. J. Heat Mass Transfer 15 (1972).
[19] P. Novelli, W. Koschel, A joint ONERA-DLR research project on high speed airbreathing propulsion, in: XIV ISABE Congress, Paper IS-093, Florence, Italy, 1999.
[20] D. Pagan, P. Molton, J. Delery, Basic experiment on a supersonic vortex flow around a missile a missile body, AIAA J. Spacecraft Rockets 29 (3) (1992) 373–378.
[21] M. Péchier, Prévisions numériques de l'effet Magnus pour des configurations de munition, PhD thesis, Université de Poitiers, 1999.
[22] N. Qin, C. Jayatunga, Algebraic turbulence modelling for vortical flows around slender bodies, in: RTO AVT Symp. on Missile Aerodynamics, Sorrento, Italy, 1998.
[23] P.L. Roe, Approximate Riemann solvers, parameter vectors and difference schemes, J. Comput. Phys. 43 (1981).
[24] S.E. Rogers, K. Both, S.M. Nash, M.D. Baker, J.P. Slotnick, M. Whitlock, H.V. Cao, Advances in overset CFD processes applied to subsonic high-lift aircraft, AIAA Paper 2000-4126, 1999.
[25] P.R. Spalart, S.R. Allmaras, A one equation turbulence model for aerodynamic flows, AIAA Paper 92-0439, 1992.
[26] P.R. Spalart, S.R. Allmaras, A one equation turbulence model for aerodynamic flows, in: La Recherche Aérospatiale, 1994, pp. 5–21.
[27] B. Van Leer, Towards the ultimate conservative scheme II: Monotonicity and conservation combined in a second order scheme, J. Comput. Phys. 14 (1974).
[28] D.L. Whithfield, Three-dimensionnal unsteady Euler equation solutions using flux vector splitting, in: CFD Workshop held at the University of Tennessee Space Institute, 1984.